

Numerical Study of Flow and Heat Transfer in a Molten Flux Layer

B. Zhao^a, S. P. Vanka^b and B. G. Thomas^c

Department of Mechanical and Industrial Engineering
University of Illinois at Urbana-Champaign,
1206 W Green Street, Urbana, IL. 61801

^aPhone: 217-244-2859, Email: bzhao@uiuc.edu

^bPhone: 217-244-8388, Email: spvanka@uiuc.edu, Fax: 217-244-6534

^cCorresponding author, Phone: 217-333-6919, Email: bgthomas@uiuc.edu, Fax: 217-244-6534

Abstract

Numerical simulations are performed to study coupled fluid flow and heat transfer in a thin liquid slag or flux layer. The steady state Navier-Stokes equations are solved using the commercial finite volume code FLUENT. The combined effects of natural convection, bottom shear velocity and strongly temperature dependent viscosity are investigated. It is found that the variation of Nu with Ra for fluxes with strongly temperature dependent viscosities is analogous to correlations for fluids with constant viscosity, but the critical Ra number for the onset of natural convection is larger. For thin layers of realistic fluxes, natural convection is suppressed, and Nu increases linearly with increase of bottom shear velocity. The increase is greater for decreasing average viscosity. The increase of Nu is slight and is only due to end effects for the flat interface shape studied here.

Keywords

computational simulation, natural convection, slag, flux layer, heat transfer, laminar flow, bottom shear, variable viscosity.

1. Introduction

Slag floats on the surface of molten metals during many different processing and refining operations, including furnaces, ladles, tundishes and molds. In addition to assisting with chemical reactions, inclusion removal and protection from air absorption, this layer plays an important role in providing thermal insulation. One process where the liquid slag layer is particularly important is the continuous casting of steel. A carefully-designed mixture of oxides is added as a powder to the top of the molten steel at regular time intervals, where it sinters and melts to form a liquid flux layer that floats above the molten metal surface. The melting and reaction rates depend on the composition (especially carbon content), porosity, and thermal properties of the flux powder. The interface between the liquid flux and the sintered solid powder floating above is at the melting temperature of the flux and is generally quite rigid or viscous relative to the liquid below. The lower surface of the liquid flux layer is at the temperature of the molten steel flowing below it, and is subjected to shear velocity and shape changes which depend on the turbulent flow conditions in the molten steel. The liquid flux is drawn into the gap between the solidifying steel shell and the mold to provide lubrication and thermal uniformity. At the vessel walls, some of the molten flux can resolidify to form a solid

slag rim, that comprises the edges of the liquid flux domain. Fig. 1 shows a vertical cross section of the continuous casting process.

Superficially, the heat loss through the flux layers increases with increasing conductivity and decreasing layer thickness. However, heat transfer through the liquid flux layer actually occurs by conduction, natural convection, forced convection and even radiation for many fluxes which are semitransparent above the sintering temperature (800-1000 °C). Quantifying this heat transfer is important yet has received little attention in previous literature. It depends on many complex interacting factors, including the powder and flux properties (viscosity, density, specific heat, latent heat, conductivity, and radiation properties such as absorption coefficient), vessel geometry, the shape and thickness of the powder and liquid flux layers, interfacial level fluctuations, and the bottom shear velocity imparted by the flowing metal below. The present work investigates this coupled fluid flow and heat transfer in the thin liquid flux layer using computational models, focusing on the effects of temperature-dependent viscosity, layer thickness, and bottom shear velocity. The results of this work will be useful for the prediction of heat transfer in processes involving floating slag, consisting of solid (powder), sintered, and molten flux layers with resolidified flux at the edges.

2. Previous Work

McDavid and Thomas (1996) performed one of the few computational studies of flow in flux layers. They simulated three-dimensional (3-D) steady, coupled fluid flow and heat transfer in the powder, liquid, and re-solidified flux layers using the finite element package, FIDAP. The steel-liquid flux interface velocity was found by iterating with a 3-D $k-\epsilon$ turbulent model of fluid flow in the nozzle and mold region of the continuous caster, until equal shear stress along the interface was achieved. The steel-flux interface shape and the rate of flux infiltration into the mold-strand gap were fixed to values measured in an operating steel caster. Temperature dependent properties were used. The converged solution matched the measured liquid flux layer thickness profile. The flow solution showed a single large recirculation region whose depth increased with increasing liquid flux conductivity and decreasing flux viscosity, owing to increased heat transfer across the layer. Like flow in the steel pool beneath it, flow within the liquid flux layer was predominantly two-dimensional in the vertical plane normal to the narrow face. The consumption of flux into the interfacial gap at the edges of the flux layer had little effect on the flow pattern over most of the domain. This work showed the importance of viscosity on the flow and thermal behavior: decreasing liquid flux viscosity caused recirculation velocity to increase and a corresponding increase of convection heat transfer. It performed only two simulations, however, and ignored natural convection effects.

Natural convection in the liquid flux layer arises because the density of the liquid flux is temperature dependent. The lower surface of the liquid flux layer is just above steel melting temperature (~ 1550 °C) while its top surface is at the melting temperature of the flux (800~1200°C) (McDavid and Thomas 1996). This large temperature gradient causes a density gradient. The unstable system breaks down as buoyancy forces set up alternate rising and falling plumes, which transport hot low-density fluid upward and cold high density fluid downward. These merge together to form Rayleigh-Benard convection cells. These natural convection cells will increase the mixing and heat transfer rate significantly beyond pure conduction. The resulting fluid flow and heat transfer in these large aspect ratio fluid layers has been studied extensively (Schluter, Lortz et al. 1965; Rossby 1969; Koschmieder and Pallas 1974; Kirchartz and Oertel 1988; Goldstein, Chiang et al. 1990). In a high-aspect-ratio vessel such as a steel-slab

caster, where the surface flow is along the length and the Rayleigh number is small, it is appropriate to assume that the fluid flow is two-dimensional with the cell axis along the width.

Booker (1976) measured heat transfer and studied convection cell structure in a high Prandtl number fluid between horizontal flat plates. The viscosity varied up to 300-fold between the top and bottom boundary temperatures. The Nusselt numbers were 12% lower than predictions of standard correlations (Rossby 1969) with the viscosity evaluated at the mean of the boundary temperatures. Mohamad and Viskanta (1992) computed 2-D laminar flow in a shallow cavity (0.1 aspect ratio) driven by surface-shear and buoyancy for a low Prandtl number fluid. The cavity was heated from below and cooled at the top, where the shear velocity was applied. The equations were solved using a finite-volume method with SIMPLE (Tannehill, Anderson et al. 1997). The results showed that the shear velocity has an insignificant effect on the heat transfer when natural convection dominates, ($Gr/Re^2 \gg 1$). Increasing shear velocity lowers heat transfer when $Gr/Re^2 \sim O(1)$ but increases heat transfer at higher velocities when forced convection dominates. Other simulations also showed that shear modified the Rayleigh-Benard convective cells generated due to heating from below (Sivaramakrishnan 2000).

Recently, Sivaramakrishnan (2000) studied the transition between natural and forced convection flow in the liquid flux layer, using the finite-element program FIDAP. Above a critical bottom shear velocity, the natural convection cells are annihilated, and the flow pattern transforms into a single large recirculation region with a lower heat transfer rate. Parametric studies on flux viscosity and bottom shear velocity were performed, but this study did not include temperature dependent properties.

The present study computes fluid flow and coupled heat transfer in a liquid flux layer, accounting for the combined effects of natural convection, bottom shear velocity and strongly temperature dependent viscosity. Computations are performed for several different commercial fluxes and bottom shear velocities in a rectangular domain, shown in Fig. 2.

3. Governing Equations and Solution Method

To compute the fluid flow and heat transfer in this problem, the steady Navier-Stokes equations including buoyant body forces are solved for mass continuity, momentum in x and y direction and the heat balance:

$$\frac{\partial u}{\partial x} + \frac{\partial v}{\partial y} = 0 \quad (1)$$

$$\frac{\partial(uu)}{\partial x} + \frac{\partial(vu)}{\partial y} = -\frac{1}{\rho_0} \frac{\partial p}{\partial x} + \frac{\partial}{\partial x} \left(\nu \frac{\partial u}{\partial x} \right) + \frac{\partial}{\partial y} \left(\nu \frac{\partial u}{\partial y} \right) + \frac{\partial \nu}{\partial x} \frac{\partial u}{\partial x} + \frac{\partial \nu}{\partial y} \frac{\partial u}{\partial y} \quad (2)$$

$$\frac{\partial(uv)}{\partial x} + \frac{\partial(vv)}{\partial y} = -\frac{1}{\rho_0} \frac{\partial p}{\partial y} + \frac{\partial}{\partial x} \left(\nu \frac{\partial v}{\partial x} \right) + \frac{\partial}{\partial y} \left(\nu \frac{\partial v}{\partial y} \right) + \frac{\partial \nu}{\partial x} \frac{\partial v}{\partial x} + \frac{\partial \nu}{\partial y} \frac{\partial v}{\partial y} + \beta \Delta T g \quad (3)$$

$$\frac{\partial(uT)}{\partial x} + \frac{\partial(vT)}{\partial y} = \frac{\partial}{\partial x} \left(\alpha \frac{\partial T}{\partial x} \right) + \frac{\partial}{\partial y} \left(\alpha \frac{\partial T}{\partial y} \right) \quad (4)$$

where $\nu = \mu(T)/\rho_0$ is the kinematic viscosity, $\alpha = k_{eff}/\rho C_p$ is the thermal diffusivity and $\Delta T = T - T_0$ is the temperature difference. It is assumed that flow in the flux layer is predominantly two-dimensional and laminar, according to the low Re numbers in Table 1. The

buoyancy effect is modeled by an extra term in the y-momentum equation (gravity direction) according to the Boussinesq approximation (Boussinesq 1903).

The above equations are solved with the commercial fluid flow package FLUENT, version 6.1 (Fluent Inc., 2003). The discretization scheme used is second order upwind for momentum and energy equations, and the SIMPLE scheme for pressure-velocity coupling. The steady state equations are solved using the segregated solver. The convergence criterion for all the simulations was 10^{-6} , which means that the scaled residual of the final solution is reduced to 10^{-6} of the initial residual (defined at the fifth iteration).

4. Code validation

The code was first validated against analytical solutions in several different problems, including flow between two parallel plates with temperature-dependent viscosity and buoyant convection in a thin layer. Excellent agreement was achieved in all cases. The code was further validated against experimental data involving steady Rayleigh-Benard convection in large-aspect ratio cavities.

Kirchartz and Oertel (1988) measured natural convection flow in a thin cavity with aspect ratio of 10:4:1 (length : width : thickness) that was heated from below. The top and bottom were copper plates kept at constant temperatures. The sidewalls were glass which has higher thermal conductivity than the fluid, silicon oil. The density variations produced by the temperature distribution were visualized using a differential interferogram.

A two-dimensional simulation was performed to match the experimental conditions for Case 1A, given in Table 1. The side walls were assumed to be perfectly conducting with a linear temperature gradient. The flow field and temperature contours obtained using a grid of 320 cells along the length and 32 cells in the thickness direction are shown in Fig. 3. The periodic high temperature gradients where the rising plumes impinge on the top surface cause increased local heat transfer rates. Fig. 4 and Fig. 5 compare the fringes of the experimental interferograms with density gradients constructed from the temperature gradients using the relation $d\rho = -\beta dT$. Both experimental and computational results show ten natural-convection cells with aspect ratio about unity and cell size equal to the domain height. The end cells are distorted due to interactions with the side walls. The simulated figures mirror the experimental figures, with the cells rotating in the opposite direction, as two symmetrical stable solutions are possible.

A series of similar simulations was then performed with adiabatic side walls by varying the liquid layer thickness. The Rayleigh number ($Ra = \rho g \beta \Delta T H^3 / (\mu \alpha)$), characterizing the strength of the natural convection, and the fluid properties, included in the Prandtl number ($Pr = \nu / \alpha$), are provided as Case 1B in Table 1. Fig. 6 compares the simulated results with measurements by Rossby (1969) for the same conditions. The Nusselt number at the top surface ($Nu = H / \Delta T \cdot \partial T / \partial y$) represents the heat transfer rate relative to pure conduction. The average Nu across the top surface increases linearly with the logarithm of Ra. There is slight deviation for Ra numbers above 10^5 , (Re numbers above ~ 1), which may be due to the onset of oscillatory convection. The good agreement seen here validates the adequacy of this computational grid and model assumptions for the simulations in this study.

5. Details of the Simulations

The domain and boundary conditions used for computations of convection in a liquid flux layer are shown in Fig. 2. The flux layer is approximated as a two-dimensional rectangular domain with a length of 0.7 m and thickness of 0.01 m. This represents a slice through the vertical plane between the narrow faces of a 1.4m wide continuous cast strand, extending from

the left narrow face to the SEN center. As discussed earlier, this two-dimensional assumption is appropriate for slab caster domains which are much longer than their width ($\sim 0.05\text{-}0.2\text{m}$), and have submerged bifurcated nozzles directed at the narrow faces that produce surface flows in this 2-D plane. The depth of the liquid flux layer develops from a balance between the melting of the powder, which depends on the rate of heat flow through the layer, and the consumption of liquid at the meniscus. This depth often varies from the narrow face to the submerged entry nozzle, according to the flow pattern of the molten steel beneath it. For this study, the flux layer thickness is assumed constant at a typical depth of 10mm. The small effect of the flux infiltration into the mold-strand gap is neglected.

Because of the steep increase in viscosity, the top of the liquid layer is approximated as a flat surface at the flux melting temperature. The lower surface is set to the molten steel temperature. The value of 1550 °C represents a superheat of about 15°C above the liquidus temperature of 1535 °C for ultra-low carbon steel (in which %C < 0.01%). The right side of the domain is a symmetry plane, so is an adiabatic, free-slip wall. The left side is in contact with the mold, which should be a wall at the flux solidification temperature. However, to avoid singularity at the left-bottom corner, and to represent the effects of flux leaking into the gap between the steel shell and the mold, the bottom half of the left wall is given a linear temperature profile. Table 2 gives the standard conditions and properties used in the simulations.

The shear velocity along the bottom steel flux interface is varied parametrically to investigate the effect on convection in the liquid flux layer. The steel velocity increases from about 0.05 to 0.4 m·s⁻¹ as casting speed increases (Thomas 2003). To match the interfacial shear stress, the liquid flux velocity is much smaller, owing to its higher viscosity. Specifically, the corresponding liquid flux velocity is about 1 to 65 mm·s⁻¹ for a typical flux with 0.2 Pa·s interface viscosity (Larson 1986), based on balancing the interfacial shear stress according to previous work (McDavid and Thomas 1996; Sivaramakrishnan 2000). The bottom velocity also varies from zero at the edges to a maximum midway between the narrowface and SEN (McDavid and Thomas 1996). In this work, constant bottom shear velocities from 0 to 200 mm·s⁻¹ are assumed.

5.1. Flux Viscosity

The viscosity of the liquid flux layer in a continuous caster varies greatly with its composition and temperature. Commercial fluxes typically contain mainly Al₂O₃ (0 ~ 13 %), CaO (22 ~ 45%), and SiO₂ (17 ~ 56%) (Branion 1987), with small amounts of fluorides (NaF, CaF₂), alkalis (Na₂O, K₂O) and other basic oxides (MgO, BaO). Increasing the SiO₂ content enhances cross linking of the silicate chains, and thereby increases viscosity (Pinheiro, Samarasekera et al. 1994). Increasing Al₂O₃ content also increases the viscosity (Pinheiro, Samarasekera et al. 1994). As Al₂O₃ is continuously absorbed into flux layer from aluminum-deoxidized steel, its content increases up to 30%. The viscosity of liquid flux decreases with temperature according to an Arrhenius equation (Pinheiro, Samarasekera et al. 1994).

$$\mu = A \exp\left(\frac{E}{RT}\right) \quad (5)$$

As the powder sinters, its viscosity increases greatly, exceeding 10⁴ Pa·s (McDavid and Thomas 1996). The inter face between the powder and the liquid often becomes crusty and enriched in carbon (Xie, Wu et al. 1991). Beneath this rigid interface, the viscosity decreases according to the increase in local temperature. Upon re-solidification against the mold at the

meniscus (left domain wall), the flux viscosity increases according to the cooling rate and its crystallinity, but this effect is beyond the scope of the present work.

There are many empirical equations for flux viscosity. Riboud and Larrecq (1979) give one such an equation, based on temperature and composition.

$$\mu = ATe^{B/T} \quad (6)$$

$$\ln A = -20.81 - 35.75x_{Al_2O_3} + 1.73x_{CaO} + 5.82x_{CaF_2} + 7.02x_{Na_2O} \quad (7)$$

$$B = 31140 + 68833x_{Al_2O_3} - 23896x_{CaO} - 46351x_{CaF_2} - 39519x_{Na_2O} \quad (8)$$

where μ is viscosity in Pa·s, T is temperature in Kelvin and x is the mole fraction of constituent compound. For a typical flux (45% SiO₂, 10% Al₂O₃, 10% CaO, 10%CaF₂, 15% Na₂O), A is 5.6^{-10} Pa·s·K⁻¹ and B is ~24,000 K. To characterize a range of fluxes for a parametric study, Eq. 6 was transformed to:

$$\mu = \mu_0 \frac{T}{T_0} e^{B\left(\frac{1}{T} - \frac{1}{T_0}\right)} \quad (9)$$

where T_0 is a reference temperature (1773 K), μ_0 is a reference viscosity (0.05 Pa·s), and B is a parameter representing the degree of temperature dependency of the flux viscosity. Fig. 7 shows various viscosity curves with this equation for different values of B , that represent the artificial fluxes simulated in this work.

This study also investigates two real industrial fluxes, commonly used in steel plants. Curves of the following form were fitted to measurements of flux viscosity taken from (Larson 1986) and (Lanyi and Rosa 1981).

$$\mu = \mu_0 \left(\frac{T_0 - T_s}{T - T_s} \right)^n \quad (10)$$

where μ_0 is the viscosity at the reference temperature, T_0 of 1300 °C, and T_s is the fitting parameter.

Fig. 8 shows the two viscosity curves. Viscosity curve (a) (Larson 1986) shows the typical behavior of a glassy flux, whose viscosity decreases smoothly with increasing temperature. Curve (b) (Lanyi and Rosa 1981) depicts a typical crystalline flux, and was chosen to investigate behavior where the viscosity drops suddenly from the solid state upon melting. Except for missing the sharp peak near the melting point, the data for this crystalline flux is also reasonably approximated using Eq. 10 with $B=23,880$ K, which is shown as curve (c) in Fig. 8.

5.2. Flux Thermal Properties

Thermal conductivity of the liquid flux layer varies over a wide range. Since the liquid flux is semitransparent, radiation upward from the lower surface (liquid steel) causes additional heat transfer. This was approximated by defining a “radiation thermal conductivity” (k_r) (Mikrovas, Argyropoulos et al. 1991; Susa, Nagata et al. 1993). This treatment is valid for “optically-thick” layers, where the product of absorption coefficient and thickness exceeds 3. This is the case for the flux layers of interest here that are 5-15mm thick, and contain at least 0.5%FeO (Taylor and Mills 1988). The conductivity (k_c) of liquid flux with only conduction is about 0.2~0.6 W·m⁻¹

$^1\cdot\text{K}^{-1}$ (Taylor and Mills 1988; Mikrovass, Argyropoulos et al. 1991). Radiation increases this significantly, depending on the steel surface temperature and flux melting temperatures (which are known), and the flux absorption properties, which are estimated. A typical value of $3\text{ W}\cdot\text{m}^{-1}\cdot\text{K}^{-1}$ is used for effective conductivity ($k_{\text{eff}} = k_c + k_r$), as assumed elsewhere (McDavid and Thomas 1996). The specific heat of the flux was assumed to be constant at $2000\text{ J}\cdot\text{kg}^{-1}\cdot\text{K}^{-1}$, as assumed elsewhere (McDavid and Thomas 1996). Buoyancy is represented by the Boussinesq approximation, (section 3) assuming a constant volumetric expansion coefficient β of $2.4\times 10^{-5}\text{ K}^{-1}$ (McDavid and Thomas 1996). For typical temperature differences across flux layers, $\beta\Delta T \ll 1$ so this approximation is valid. Thus, a constant density of $2500\text{ kg}\cdot\text{m}^{-3}$ was adopted.

6. Results and discussion

6.1. Grid refinement study

To investigate grid independence, simulations were performed for two grids, 640×32 and 1280×64 , assuming bottom shear velocity of $0.01\text{ m}\cdot\text{s}^{-1}$ and viscosity curve (a) in Fig. 8. Fig. 9 compares the velocity and temperature profiles near the right wall, where the largest gradients are found. The results differ by less than 1%, so the 640×32 mesh is used for the remaining calculations.

6.2. Effect of temperature dependent flux viscosity

The effect of temperature dependent flux viscosity on natural convection was first studied with 13 simulations, based on Eq. 10 with B values ranging from 5,000 K to 23,880 K. The assumed viscosity curves (Fig. 7) represent variations on a real flux (B~24,000 K) but with decreasing temperature dependency, and corresponding decreasing viscosity at the upper interface (1000°C). A case with an extremely low constant viscosity of $0.05\text{ Pa}\cdot\text{s}$ was also performed. These simulations were done with zero bottom shear velocity in order to first study just the effect of viscosity variations. Other parameters, including domain thickness were constant, as given in Table 2.

The flow, temperature and viscosity fields of the flux layer with intermediate temperature variation of viscosity (B=10,000 K) is shown in Fig. 10. The results are generally similar to the classic Rayleigh-Benard convection pattern given in Fig. 3 for a constant viscosity. The size of the convection cells, based on the distance between the eyes of the vortices at the center of adjacent cells, is roughly equal to the domain height. The cell shape is roughly square, so the number of cells depends on the aspect ratio of the domain. Slight differences in flow, temperature and cell shape arise at the domain ends, owing to the different boundary conditions at the side walls. However, these end effects are insignificant due to the large aspect ratio of the domain. More importantly, with constant viscosity, the upward and downward plumes have the same strength, so the velocity and temperature fields have the same shape when inverted. The viscosity variation weakens the convection, and lowers the maximum velocity to $\sim 1\text{ mm}\cdot\text{s}^{-1}$, compared with $2\text{ mm}\cdot\text{s}^{-1}$ with the constant viscosity case of $0.05\text{ Pa}\cdot\text{s}$. This damping of the convection reduces the temperature gradients and heat transfer. If the viscosity – temperature relationship was linear, then the viscosity and temperature fields would appear the same. However, the nonlinear viscosity variation with temperature also causes the appearance of the viscosity field to differ from the temperature field.

As the viscosity variation is increased (increasing B), the higher viscosity progressively weakens natural convection until the convection cells completely disappear. Fig. 11 shows

results for the strong viscosity variation of a typical real flux ($B=23,880$ K), where natural convection is suppressed. The velocity field is almost stagnant. The maximum velocity is only $\sim 0.1 \text{ mm}\cdot\text{s}^{-1}$, caused only by the boundary condition at the left wall. The nearly linear temperature field corresponds to pure conduction with the minor end effect.

6.3. Effect of Flux Layer Thickness

Increasing thickness of the liquid flux layer promotes natural convection. The effect of increasing flux layer thickness was investigated for thicknesses between ~ 10 mm and ~ 20 mm for a real flux (curve c in Table 3 and Fig. 7) and other conditions given in Table 2. Fig. 12 shows results for the same conditions as Table 2 except that the layer thickness is increased to 15.92 mm. With the increased thickness, the natural convection is no longer completely suppressed. The maximum velocity increases to $1 \text{ mm}\cdot\text{s}^{-1}$. The shape of the convection cells changes, as flow is restricted mainly to the lower part of the domain where the fluid is less viscous. Flow in the top portion is nearly stagnant. Each convection cell is smaller, and has a width to height aspect ratio of only 0.63, if the inactive region at the top of the cell is included.

6.4. Heat Transfer Rates

The rate of heat transfer through the flux layers is presented in Fig. 13 in terms of the average Nusselt number across the top surface as a function of the Rayleigh number. Results for the two sets of simulations (varying B and varying thickness) are compared with theoretical and experimental values for constant viscosity. The classic results for constant viscosity increase Ra by increasing domain thickness and / or temperature difference across the layer. For the set of simulations with varying temperature dependency, increasing Ra is obtained by decreasing the value of B , which decreases the average viscosity (while other parameters are constant, as given in Table 2). For the second set of simulations, the Ra is increased by increasing the domain thickness (while viscosity is held the same at $B=23,880$ K). As expected, natural convection increases by a factor of 2 or 3 with increasing Ra . For a fluid with variable viscosity, a characteristic viscosity is needed to define the Ra number. Following (Booker 1976) the Rayleigh number was evaluated here using the viscosity at the mean temperature of top and bottom boundaries (1275°C).

Based on linear stability theory, the minimum Rayleigh number to start natural convection, Ra_c , is 1707 for a constant viscosity fluid (Schluter, Lortz et al. 1965). For the fluids with temperature dependent viscosity considered in this work, the critical Ra number was determined by fitting the simulation results to the following Nu - Ra correlation developed for constant-viscosity large- Pr fluids (Schluter, Lortz et al. 1965):

$$\frac{Ra(Nu-1)}{Ra-Ra_c} = C \quad (11)$$

This equation is only valid for Ra larger than Ra_c and less than about $3 Ra_c$. The constant C increased from 1.43 for constant viscosity (Schluter, Lortz et al. 1965) to 1.827 for the variable viscosity case. The critical Ra number, at the $Nu=1$ intercept (pure conduction), increased to 2285. The higher critical Rayleigh number is consistent with the higher viscosity region suppressing natural convection cells. Basing the viscosity on the average temperature and using Eq. 11 with $C=1.43$ underestimates this critical Ra , which agrees with similar findings based on experiments by (Booker 1976). As Ra increases, the temperature dependency of the viscosity

decreases, becoming closer to a constant viscosity, so the curve approaches the constant viscosity curve.

It is further seen that the critical Ra for changing flux layer thickness is 2403 and the curve is translated to the right, relative to constant viscosity results. This critical Ra exceeds that of the other sets as expected, because it was based on the viscosity function with the largest value ($B=23,880$ K). The constant in Eq. 11 increases to 1.446. The curve based on temperature-dependent viscosity falls between the curves based on constant viscosity and variable layer thickness. These results demonstrate that Ra number alone does not provide sufficient information to characterize the natural convection strength for real fluids where viscosity varies with temperature.

6.5. Effect of bottom shear velocity

In a real steel caster, the liquid flux layer floating on top of the steel free surface in the mold is always subject to a shear velocity on its bottom surface. This shear velocity greatly affects flow and heat transfer in the liquid flux. Increasing this velocity causes the steel flux interface to become wavy, with flow and thickness variations known as “level fluctuations”. If it becomes too large, liquid flux may be entrained into molten steel to form inclusion defects in the final product. The shear velocity also greatly affects heat conduction across the flux layer. In this work, we have investigated the effect of controlled shear velocity on the convection in the liquid flux layer. The bottom surface is assumed to remain flat with a constant domain thickness. Simulations are performed for the three viscosity curves for real fluxes given in Table 3 and Fig. 8.

The Rayleigh numbers calculated for viscosity curves (a), (b), and (c) (based on the viscosity at the average temperature) are 353, 1375 and 1239 respectively. The results in Fig. 13 show that the Ra numbers for all three cases are below the smallest critical Ra number, so no natural convection cells are expected. Applying shear velocity to the bottom surface further suppresses the formation of natural convection cells. The simulation results confirm this for all cases.

Fig. 14 shows typical flow, temperature and viscosity fields for the liquid flux layer (corresponding to viscosity curve (a)) subjected to a bottom shear velocity of $0.1 \text{ m}\cdot\text{s}^{-1}$. The results for all three viscosity curves are very similar. This shows that accurate modeling of the sharp increase in viscosity near the solidification temperature is not important, which is logical for very high viscosities. The flow fields share the common feature of one large recirculation region. The temperature fields feature larger temperature gradients at the right end of the domain caused by upward turning of the flow and almost pure conduction in the center region. This is because the flow is essentially stratified and laminar, so there is no vertical mixing or convective heat transfer.

In simulations shown in Figs. 10 and 12 where there is natural convection, the heat transfer rate varies in an oscillatory manner across the length of the top surface. The peaks and valleys correspond to upward and downward moving plumes. When the bottom shear velocity generates a single recirculation loop, the heat transfer across the domain is greatly skewed, with a large (negative) maximum towards the right wall on the top surface. The bottom surface has an even larger maximum at the lower left corner. These skewed distributions, shown in Fig. 15, should be considered, in addition to the average heat transfer.

The effect of bottom shear velocity on the horizontal velocity profile at the center of the domain is shown in Fig. 16 for viscosity curve (a). The interior velocities logically increase with bottom shear velocity. The flow direction changes at a height of 16-20% of the layer thickness.

The height of this eddy center increases slightly with bottom shear velocity. Above 0.0086 m, the velocity diminishes to zero due to the high viscosity in this region. This makes the profile deviate from the parabolic profile of Couette flow. The vertical velocities are negligible, owing to the large aspect ratio of the domain.

The corresponding temperature profiles are shown in Fig. 17. With small bottom shear velocity, the flow at the domain ends does not affect flow near the center, so the temperature profile is linear as in pure conduction. With increasing bottom shear velocity, the end effects extend towards the center and the temperature profile departs from linearity. Fig. 18 shows the viscosity profiles, which vary nonlinearly according to the temperature.

The effect of different flux viscosity curves on the velocity profile is shown in Figs. 19 and 20. The relationship between shear stress and bottom velocity is given in Fig. 21, is computed from these results. In addition to the flux viscosity profile, this relationship depends on thickness of the flux layer, (10 mm here) and the interface temperature. The interface temperature is that of the molten steel, which is always around 1550 °C. This figure also shows the corresponding velocities in the steel near the top of the molten pool, just outside the boundary layer at the interface. These were computed using the logarithmic relationship for turbulent boundary layers (McDavid and Thomas 1996; Sivaramakrishnan 2000).

For conditions of constant shear stress across the bottom surface, Fig. 20 shows that the velocities increase greatly from flux (a) to (b) to (c). This is due to the decreasing bottom surface viscosity, from flux curves (a) to (b) to (c). The average viscosity is actually lowest for flux (b), owing to its higher average temperature in the domain. The results are compared in Fig. 19 for constant bottom shear velocity. The height of the eddy center is highest for flux (b) (0.0024 m), owing to its viscosity profile (Fig. 8) which is relatively constant over most of the domain, except for the sharp increase at the very top. For the same reason, the stagnant region near the top is smaller with viscosity curve (b). The temperature profiles appear similar for all three fluxes and deviate only slightly from linearity for practical values of bottom shear velocity.

In the absence of natural convection cells, the flow pattern with a steady bottom shear velocity in this rectangular domain is stratified and there is no convective heat transfer, except near the ends. The rate of heat transfer, expressed in terms of Nu number, is shown in Fig. 22 as a function of bottom shear velocity. It can be seen that Nu increases almost linearly with shear velocity. This is due to extension of the end effects with increasing circulation velocity in the domain. The rate of increase depends on the viscosity. The Nu number increases fastest for case (b), which has smallest average viscosity, and slowest for case (a), which has largest. This is because the end effect extends farther for the lower viscosity. The corresponding results with velocity in the molten steel are shown in Fig. 23. The trends are similar, except the curves increase logarithmically, owing to the nonlinear relationship between interface shear stress and velocity in the turbulent steel (Fig. 21).

The increase in heat transfer rate with interface shear velocity agrees with previous findings (McDavid and Thomas 1996; Sivaramakrishnan 2000). It is expected from operating experience that increasing steel velocity increases heat transfer in the liquid flux pool. This in turn increases the melting rate at the flux / powder interface and increases the liquid flux layer thickness.

The maximum Nu, for bottom shear velocity of $0.2 \text{ m}\cdot\text{s}^{-1}$, is only about 2.3. Most liquid flux layers are subject to shear velocity less than $0.05 \text{ m}\cdot\text{s}^{-1}$, where the Nu is less than 1.3. These small values show that forced convection from the bottom shear velocity produces only modest increases in heat transfer above the value for pure conduction. It is much smaller than the increase resulting from natural convection. This work suggests that plant observations of larger

increases are likely due to phenomena not considered here. These include transient oscillations suggested by the higher Re numbers in Table 3), fluctuations and break-up of the bottom interface shape, caused by bubble motion, turbulent flow of the molten metal beneath the layer, and even slag emulsification. In addition, higher or time-varying recirculation velocities in the domain may enhance mixing within the sintering flux above the top interface. This would increase the local kinetics of melting, resulting in higher effective conductivity, and a thicker liquid layer. Such phenomena should be investigated in future work.

7. Summary

Computational models are used to simulate 2-D fluid flow and heat transfer in the liquid flux layer above a molten metal surface, such as encountered in the continuous casting of steel. The model includes the effects of natural convection, temperature-dependent viscosity, and shear velocity across the bottom surface. It is found that the Ra number for realistic liquid slag layers varies near the critical Ra number for the onset of natural convection. For fluxes with temperature-dependent viscosity, the variation of Nu with Ra is analogous to correlations for fluids with constant viscosity evaluated at the mean temperature, but the critical Ra number is larger. The increase in Nu number with layer thickness is also quantified for realistic fluxes.

For thin layers of realistic fluxes, natural convection is suppressed, so Nu increases linearly with increase of bottom shear velocity. The increase is greater with decreasing average viscosity. The increase of heat transfer above pure conduction is only due to end effects, and hence depends on the dimensions of the layer. For the flat interface shape investigated here, this increase is only one to three fold. Larger increases observed in practice could be due to phenomena not included in these computations.

Acknowledgements

The authors thank the National Science Foundation (Grant DMI-01-15486) which made this research possible. The work is also supported by the member companies of the Continuous Casting Consortium at University of Illinois at Urbana-Champaign (UIUC). Special thanks are due to National Center for Supercomputing Applications (NCSA) at UIUC for computational facilities and to FLUENT, Inc. for the FLUENT code.

References

- Fluent V6.1. (2003). Fluent Inc., Lebanon, New Hampshire, www.fluent.com.
- Booker, J. R. (1976). Thermal Convection with Strongly Temperature-dependent Viscosity. *J. Fluid Mech.* **76**: 741-754.
- Boussinesq, J. (1903). *Théorie analytique de la chaleur*. Paris: Gathier-Villars **2**.
- Branion, R. V. (1987). *Mold Flux for Continuous Casting*. Iron and Steel Society.
- Goldstein, R. J., H. D. Chiang, et al. (1990). High-Rayleigh-number Convection in a Horizontal Enclosure. *J. Fluid Mech.* **213**: 111-126.
- Kirchartz, K. R. and H. Oertel, Jr. (1988). Three-dimensional thermal cellular convection in rectangular boxes. *J. Fluid Mech.* **192**: 249-186.
- Koschmieder, E. L. and S. G. Pallas (1974). Heat Transfer Through a Shallow, Horizontal Convecting Fluid Layer. *Int. J. Heat Mass Transfer* **17**: 991-1002.
- Lanyi, M. D. and C. J. Rosa (1981). Viscosity of Casting Fluxes Used During Continuous Casting of Steel. *Metallurgical and Materials Transactions B* **12B**: 287-298.
- Larson, D. (1986). Criteria for Selecting Mold Powders to Optimize Continuous Cast Steel Quality. *Industrial Heating* **53**: 16-19.
- McDavid, R. M. and B. G. Thomas (1996). Flow and Thermal Behavior of the Top Surface Flux/Powder Layers in Continuous Casting Molds. *Metallurgical and Materials Transactions B* **27B**: 672-685.
- Mikrovas, A. C., S. A. Argyropoulos, et al. (1991). Heat Transfer Characteristics of Molten Slags. *Ironmaking and Steelmaking* **18**(3): 169-182.
- Mohamad, A. A. and R. Viskanta (1992). Laminar Flow and Heat Transfer in Rayleigh-Benard Convection with Shear. *Phys. Fluids A* **4**(10): 2131-2140.
- Pinheiro, C. A., I. V. Samarasekera, et al. (1994). *Mold Flux for Continuous Casting of Steel*. Iron and Steel Maker: 12-14.
- Riboud, P. V. and M. Larrecq (1979). *Steelmaking Proceedings*. ISS-AIME **62**(1979): 78-92.
- Rosby, H. T. (1969). A Study of Benard Convection with and without Rotation. *J. Fluid Mech.* **36**: 309-335.
- Schluter, A., D. Lortz, et al. (1965). On the Stability of Steady Finite Amplitude Convection. *J. Fluid Mech.* **23**: 129-144.

Sivaramakrishnan, S. (2000). Large Eddy Simulation, Particle Image Velocimetry in the Study of Mold Transients in Continuous Casting of Steel and Heat Transfer through Molten Slag Layers. M.S. Thesis, University of Illinois at Urbana-Champaign.

Susa, M., K. Nagata, et al. (1993). Absorption Coefficients and Refractive Indices of Synthetic Glassy Slags Containing Transition Metal Oxides. *Ironmaking and Steelmaking* **20**(5): 372-378.

Tannehill, J. C., D. A. Anderson, et al. (1997). *Computational Fluid Mechanics and Heat Transfer* (Second Edition). Taylor & Francis, Washington.

Taylor, R. and K. C. Mills (1988). Physical Properties of Casting Powders: Part3 Thermal Conductivities of Casting Powders. *Ironmaking and Steelmaking* **15**(4): 187-194.

Thomas, B. G. (2003). Continuous Casting Operation: Fluid Flow. Making, Shaping and Treating of Steel: Continuous Casting, A. Cramb, AISE Steel Foundation, Pittsburgh, PA **5**: 14.1-14.41.

Xie, B., J. Wu, et al. (1991). Study on Amount and Scheme of Carbon Mixed in CC Mold Fluxes. *Steelmaking Conference Proceedings* **74**: 647-651.

Table 1 Parameters for validation cases

Table 2 Parameters for variable viscosity and thickness simulations

Table 3 Parameters for shear velocity simulations

Fig. 1 Schematic of mold flux layer

Fig. 2 Simulation domain and boundary conditions

Fig. 3 Velocity and temperature fields of Rayleigh-Benard convection (Case 1A)

Fig. 4 Contours of vertical density gradient, above from numerical simulation (Case 1A), bottom from experiment (Kirchartz and Oertel 1988)

Fig. 5 Contours of horizontal density gradient, above from numerical simulation (Case 1A), bottom from experiment (Kirchartz and Oertel 1988)

Fig. 6 Change of Nu with respect to Ra (Case 1B)

Fig. 7 Flux viscosity curves used for variable viscosity study

Fig. 8 Viscosity of two real fluxes (measured points) and three models approximations (lines)

Fig. 9 Temperature and velocity profile from grid refinement study ($x=0.695\text{m}$, viscosity curve a and $u_b=0.01\text{ m}\cdot\text{s}^{-1}$)

Fig. 10 Flow, temperature and viscosity field of liquid flux layer with variable viscosity ($B=10000$)

Fig. 11 Flow, temperature and viscosity field of liquid flux layer with variable viscosity ($B=23880$)

Fig. 12 Flow, temperature and viscosity field of liquid flux layer with variable viscosity ($B=23880$, modified thickness, $Ra=5,000$)

Fig. 13 Heat flow increase as a function of convection strength (symbols are computations and lines are curve fits)

Fig. 14 Velocity field (top); temperature field (middle) and Viscosity field (bottom) of liquid flux layer with variable viscosity (a) and bottom shear velocity $0.1\text{ m}\cdot\text{s}^{-1}$

Fig. 15 Nu distribution on the top and bottom of flux layer (viscosity a and bottom shear velocity $0.1\text{ m}\cdot\text{s}^{-1}$)

Fig. 16 Velocity profile across the domain thickness (centerline; flux a)

Fig. 17 Temperature profile across the domain thickness (centerline; flux a)

Fig. 18 Viscosity profile across the domain thickness (centerline; flux a)

Fig. 19 Effect of flux viscosity on the velocity profile ($u_b=0.06\text{ m}\cdot\text{s}^{-1}$)

Fig. 20 Effect of flux viscosity on the velocity profile (interfacial shear stress equals $5\text{ N}\cdot\text{m}^{-2}$)

Fig. 21 Relationship between interfacial shear stress and flux/steel velocity

Fig. 22 Nu number as a function of bottom shear velocity

Fig. 23 Nu number as a function of steel velocity

Table 1 Parameters for validation cases

	Case 1A	Case 1B
Domain Length L (m)	0.1	0.111125
Domain Thickness H (m)	0.01	0.0054 ~ 0.01465
Density ρ (kg·m ⁻³)	1000	960.3
Molecular Viscosity μ (Pa·s)	0.178	0.0195
Thermal Conductivity k (W·m ⁻¹ ·K ⁻¹)	0.1	0.14154
Specific Heat C_p (J·kg ⁻¹ ·K ⁻¹)	1000	1453.2
Thermal Expansion Coefficient β (K ⁻¹)	0.001453	0.00107
Temperature Difference ΔT (K)	5	5
Gravity Constant g (m·s ⁻²)	9.8	9.8
Pr Number $\mu/(\rho\alpha)$	1780	200.21
Ra Number $\rho g \beta \Delta T H^3 / (\mu \alpha)$	4000	4000 ~ 80000
Re Number $v_{\max} H \rho / \mu$	0.01	0.01 ~ 0.82

Table 2 Parameters for variable viscosity and thickness simulations

Domain Length L (m)	0.7
Domain Thickness H (m)	0.01
Density ρ (kg·m ⁻³)	2500
Viscosity μ (Pa·s)	f(T)
Thermal Conductivity k_{eff} (W·m ⁻¹ ·K ⁻¹)	3
Specific Heat C_p (J·kg ⁻¹ ·K ⁻¹)	2000
Thermal Expansion Coefficient β (K ⁻¹)	2.4×10^{-5}
Top temperature, T_c (°C)	1000
Bottom temperature, T_h (°C)	1550
Reynolds Number, $v_{\max} H \rho / (\mu = .05)$	1.04

Table 3 Parameters for shear velocity simulations

	Flux (a)	Flux (b)	Flux (c)
Equation	9	9	10
B	-	-	23,880
Reference viscosity μ_0 (Pa·s)	0.87	0.39	0.05
Reference temperature T_0 (°C)	1300	1300	1550
Solidification Temperature T_s (°C)	850	1125	-
n	3.2	1.3	-
Top temperature T_c (°C)	850	1125	1000
Bottom temperature T_h (°C)	1550	1550	1550
Reynolds number $v_{\max} H \rho / \mu_0$	23.4	40.4	100.0

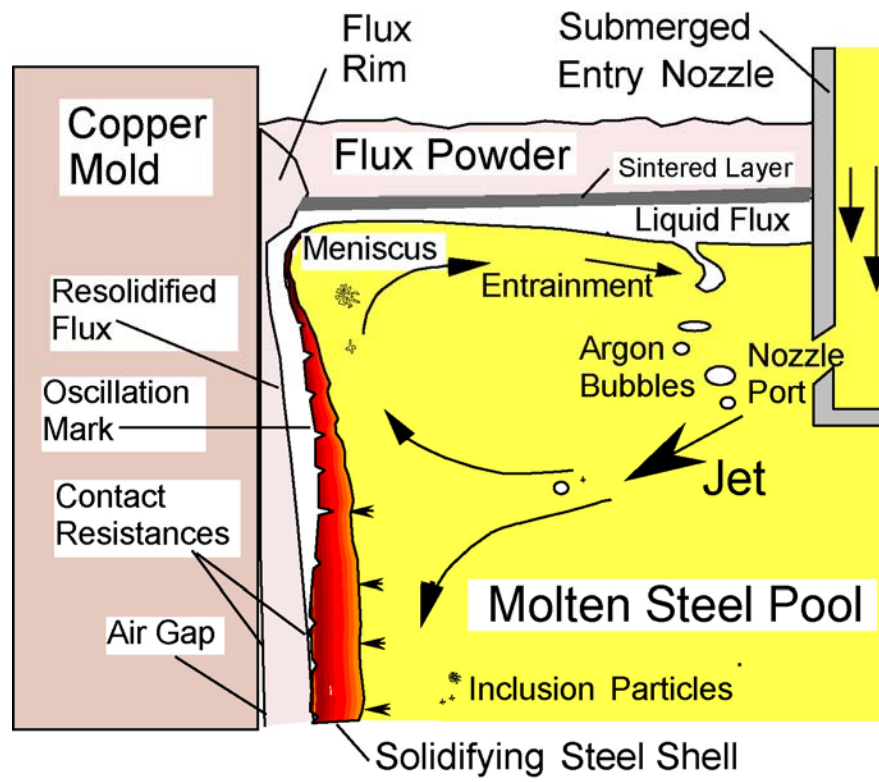


Fig. 1 Schematic of mold flux layer

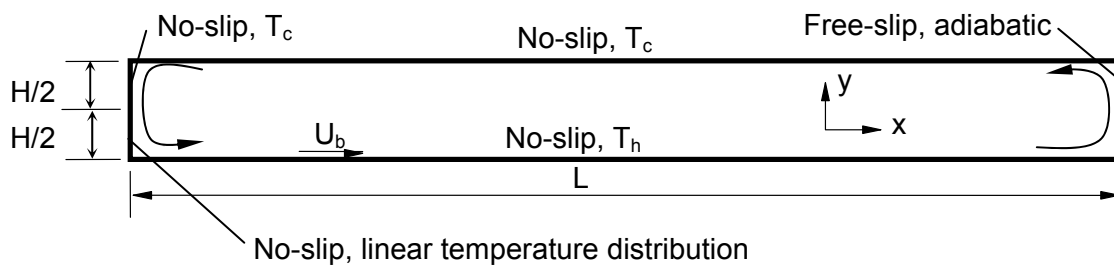


Fig. 2 Simulation domain and boundary conditions

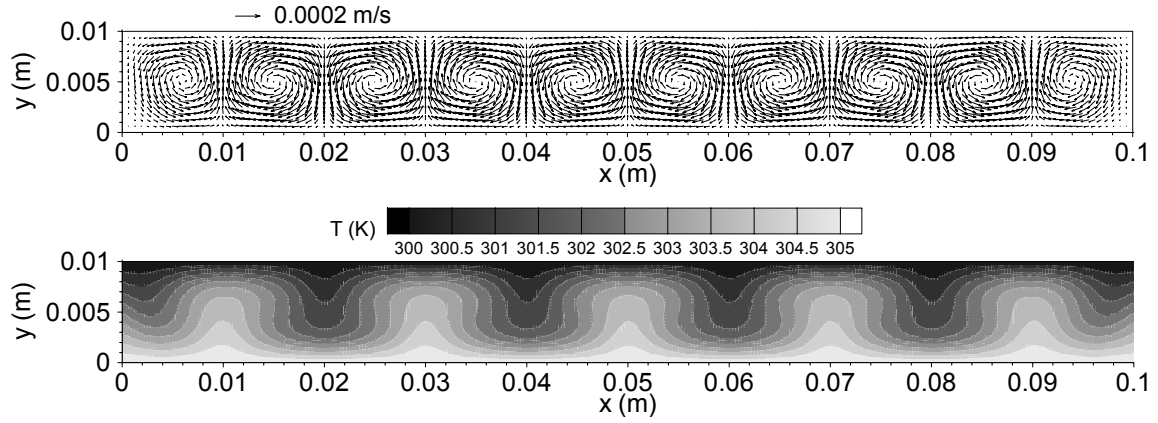


Fig. 3 Velocity and temperature fields of Rayleigh-Benard convection (Case 1A)

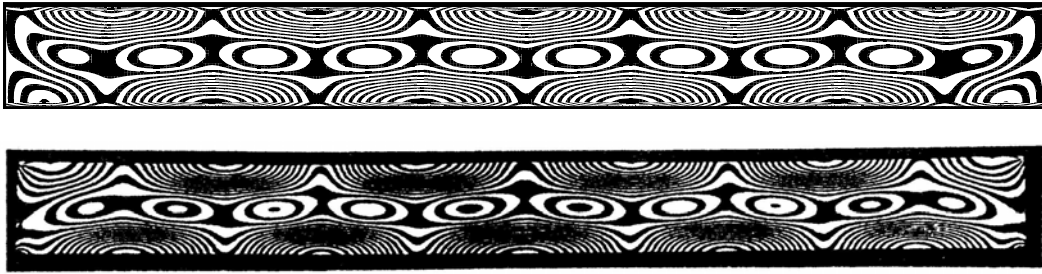


Fig. 4 Contours of vertical density gradient, above from numerical simulation (Case 1A), bottom from experiment (Kirchartz and Oertel 1988)

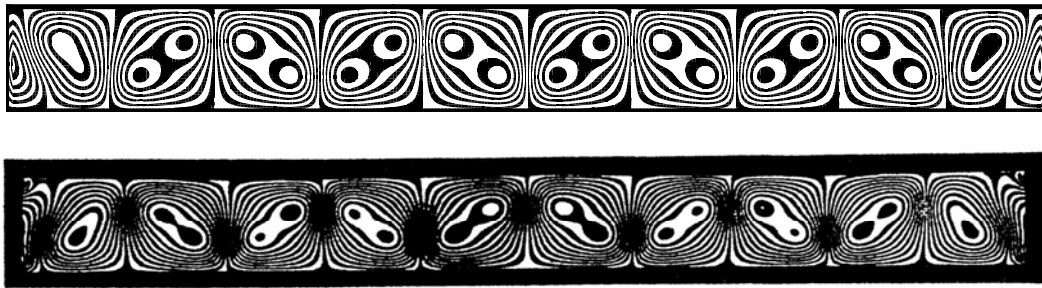


Fig. 5 Contours of horizontal density gradient, above from numerical simulation (Case 1A), bottom from experiment (Kirchartz and Oertel 1988)

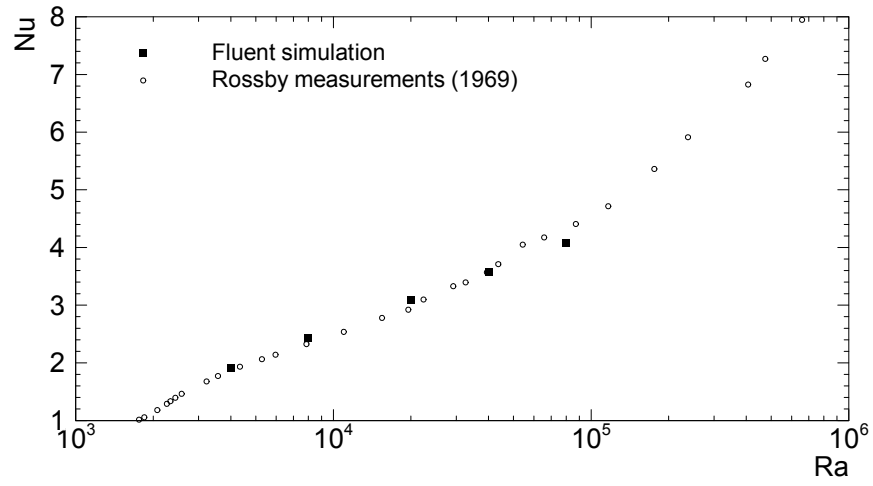


Fig. 6 Change of Nu with respect to Ra (Case 1B)

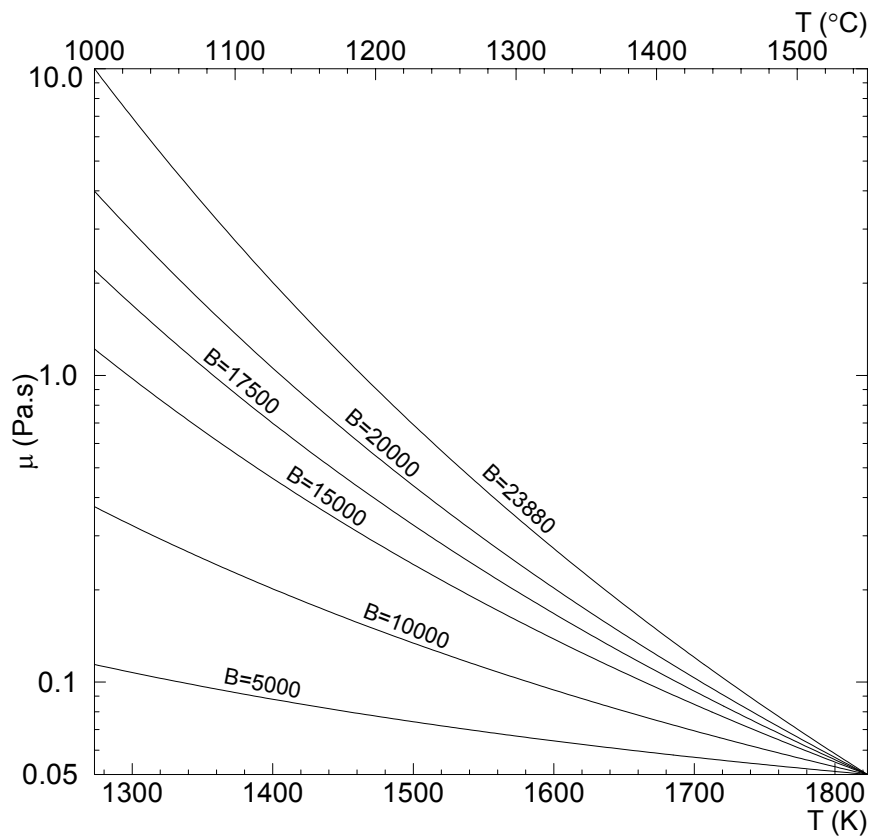


Fig. 7 Flux viscosity curves used for variable viscosity study

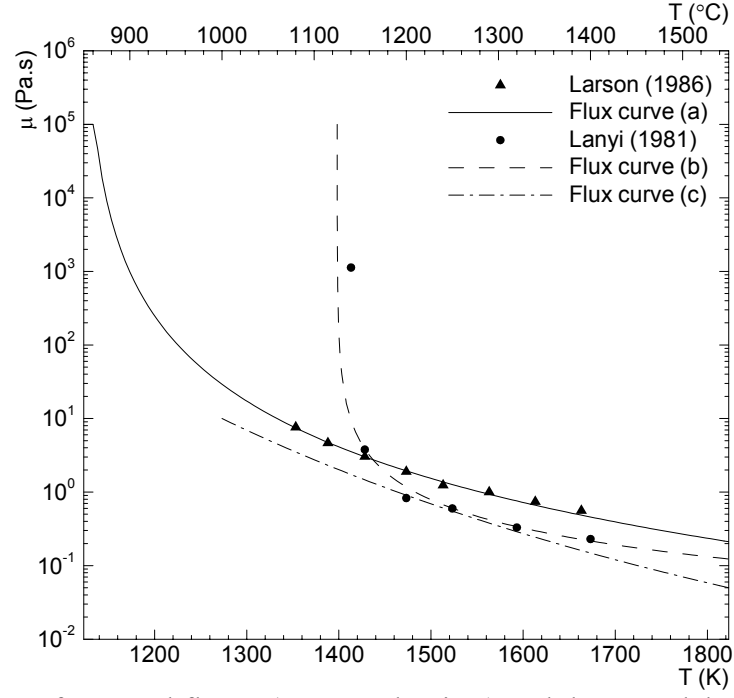


Fig. 8 Viscosity of two real fluxes (measured points) and three models approximations (lines)

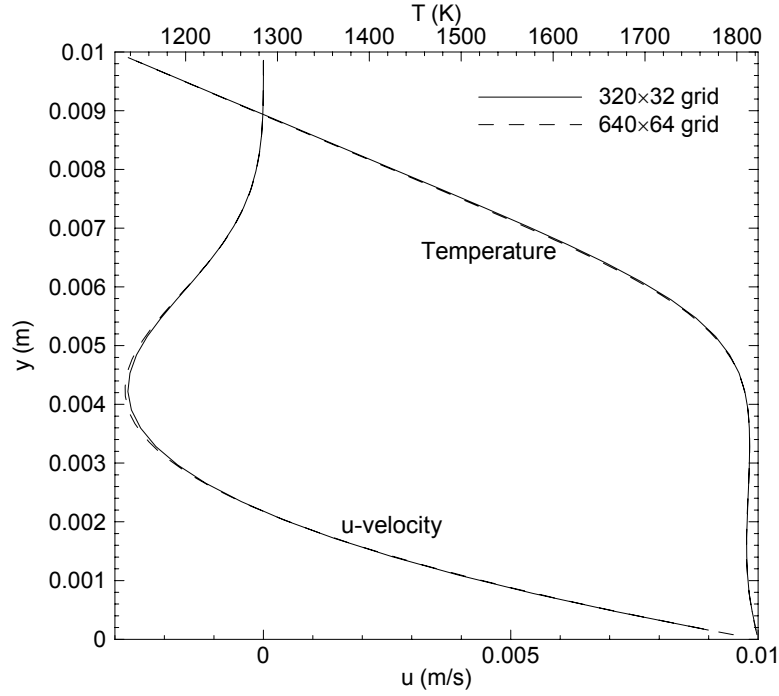


Fig. 9 Temperature and velocity profile from grid refinement study ($x=0.695\text{m}$, viscosity curve a and $u_b=0.01\text{ m}\cdot\text{s}^{-1}$)

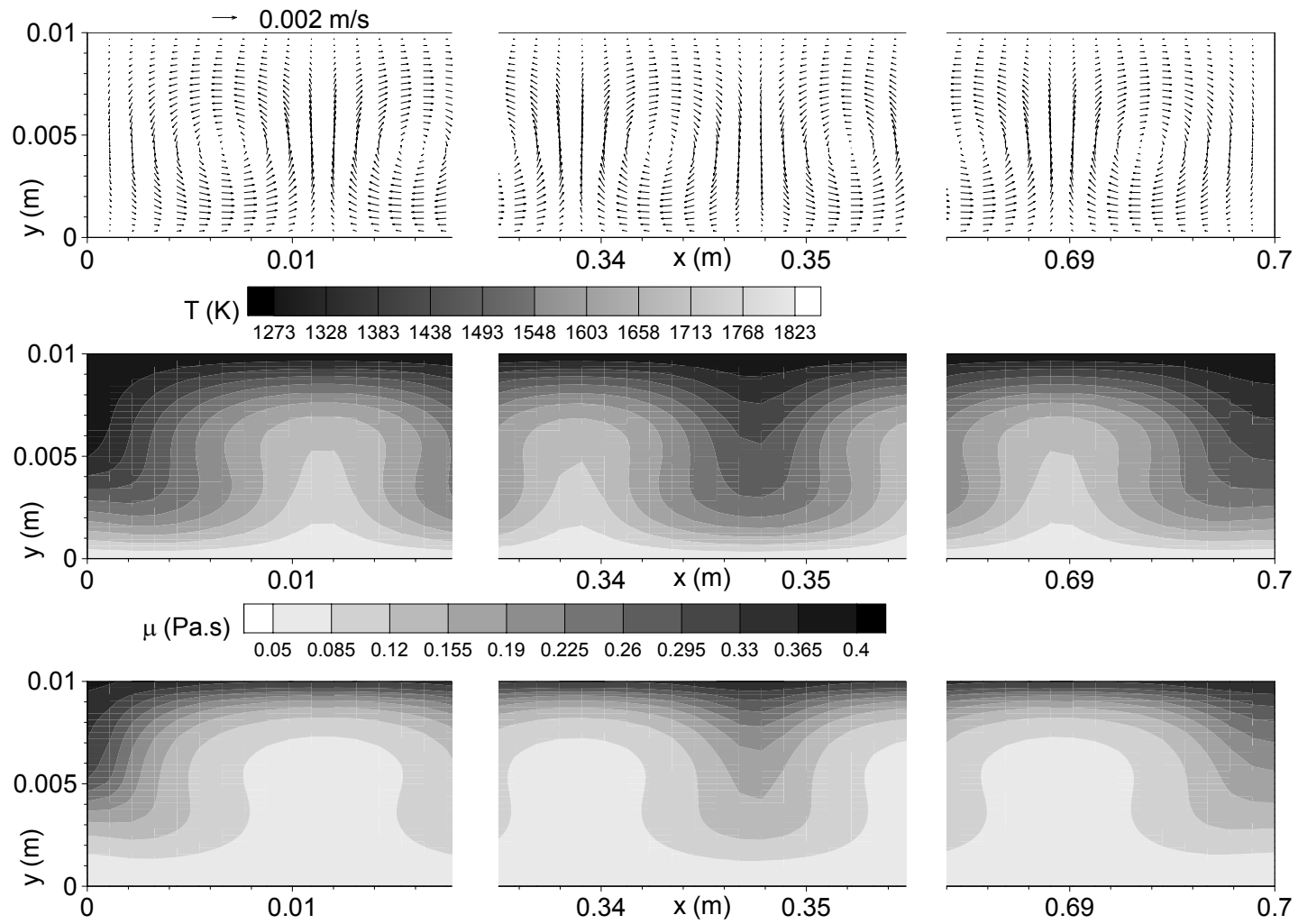


Fig. 10 Flow, temperature and viscosity field of liquid flux layer with variable viscosity ($B=10000$)

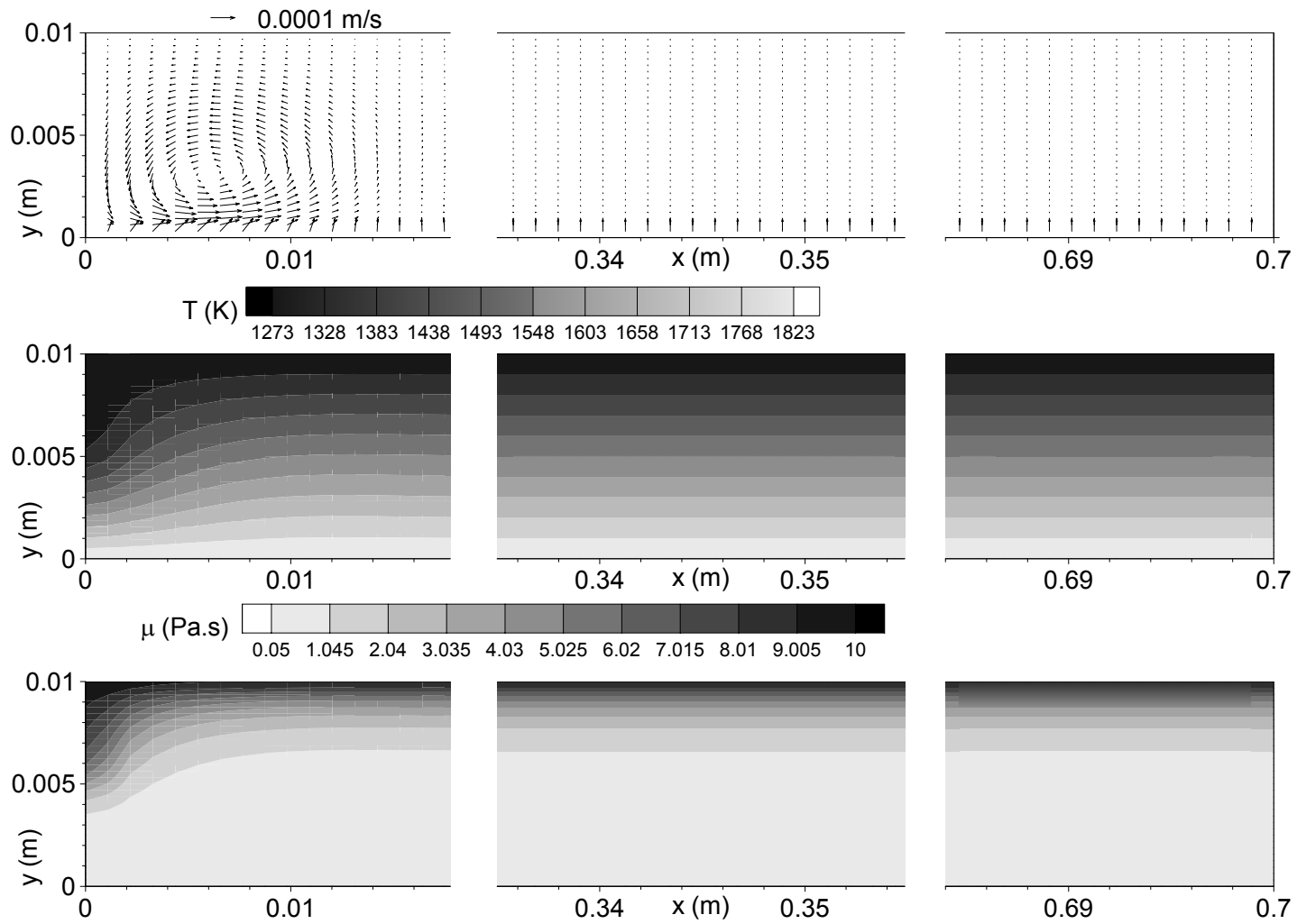


Fig. 11 Flow, temperature and viscosity field of liquid flux layer with variable viscosity ($B=23880$)

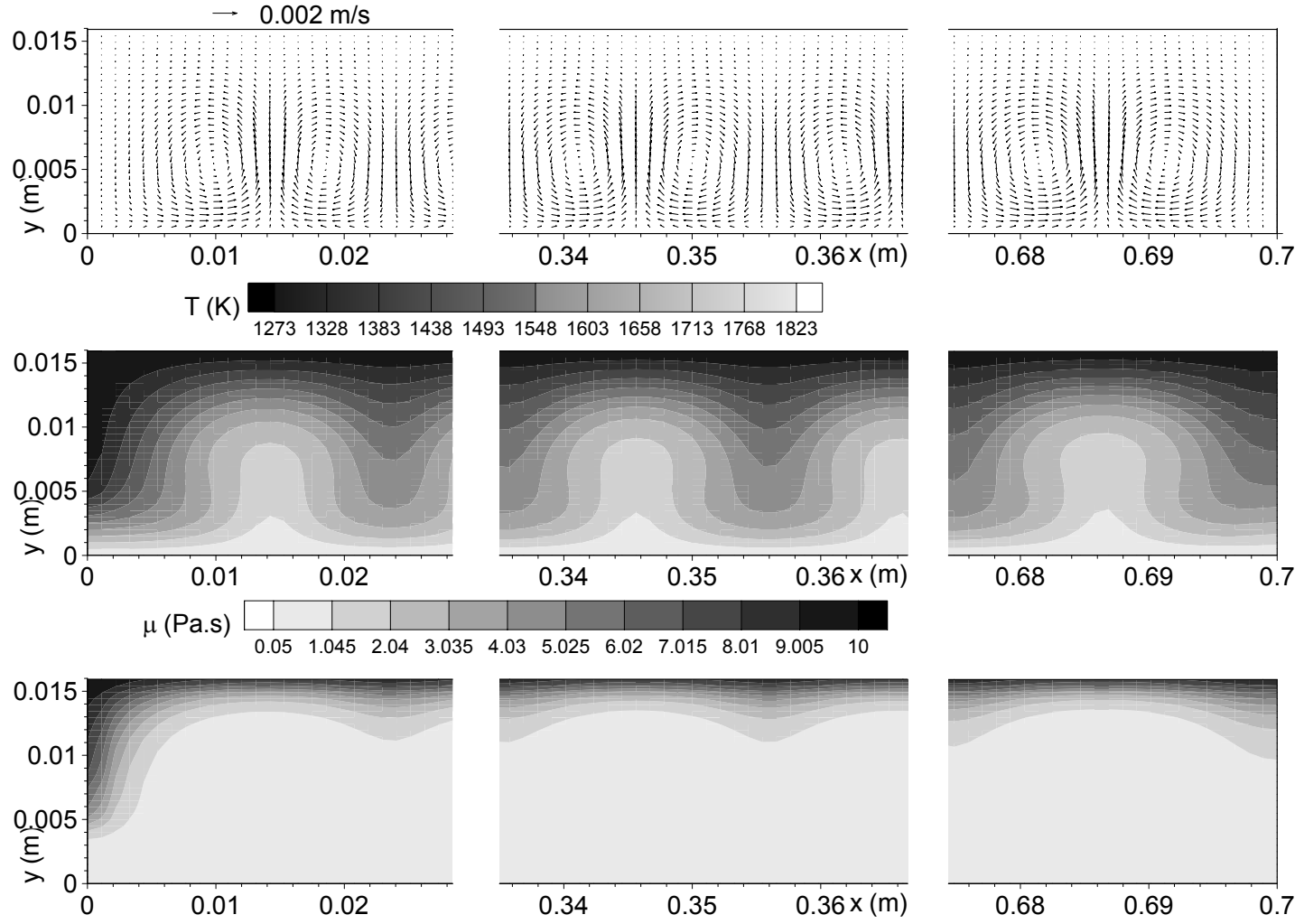


Fig. 12 Flow, temperature and viscosity field of liquid flux layer with variable viscosity ($B=23880$, modified thickness, $Ra=5,000$)

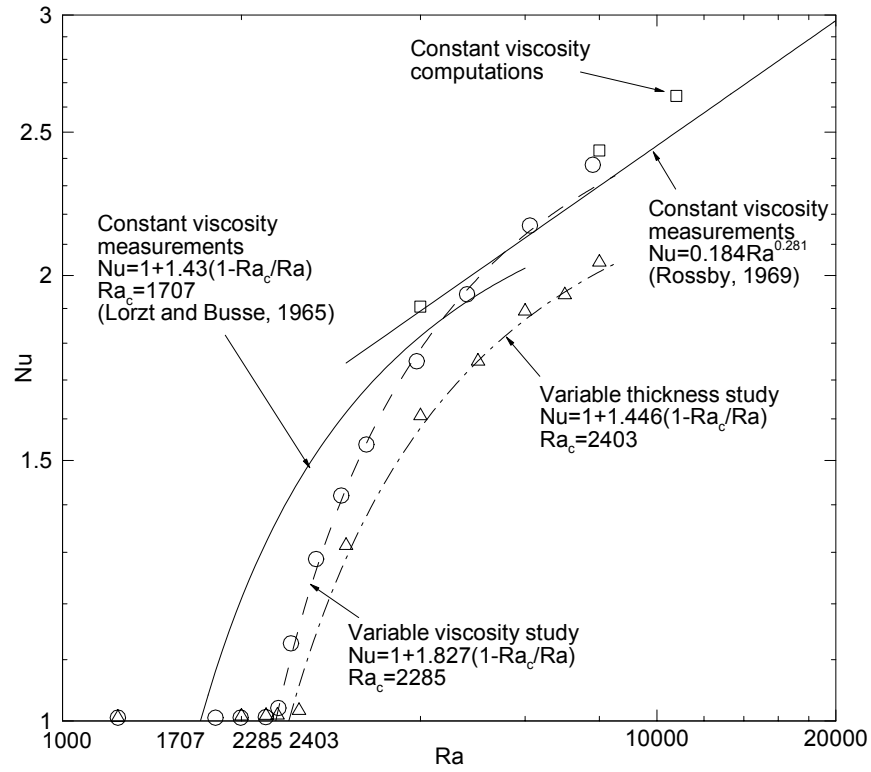


Fig. 13 Heat flow increase as a function of convection strength (symbols are computations and lines are curve fits)

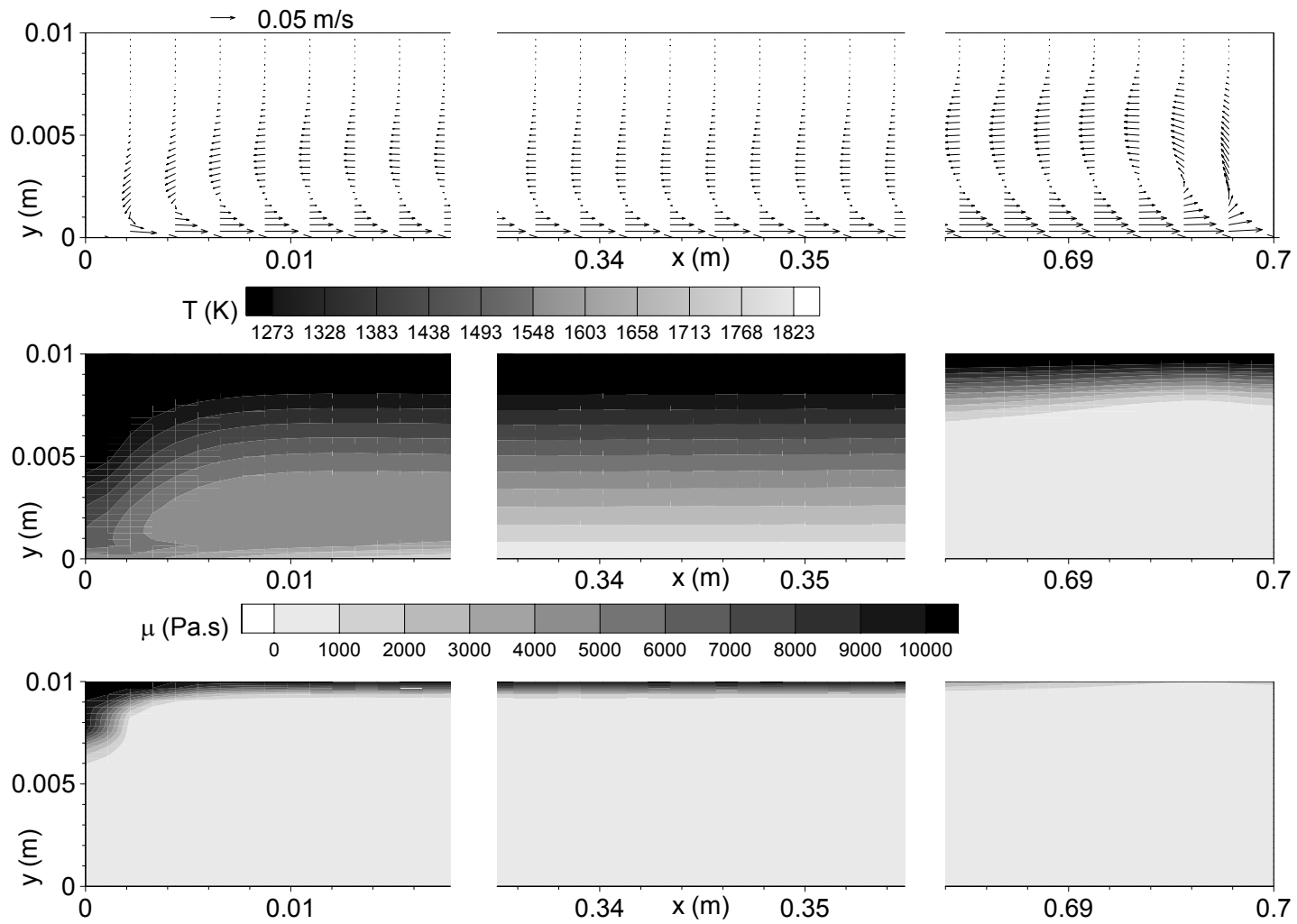


Fig. 14 Velocity field (top); temperature field (middle) and Viscosity field (bottom) of liquid flux layer with variable viscosity (a) and bottom shear velocity $0.1 \text{ m}\cdot\text{s}^{-1}$

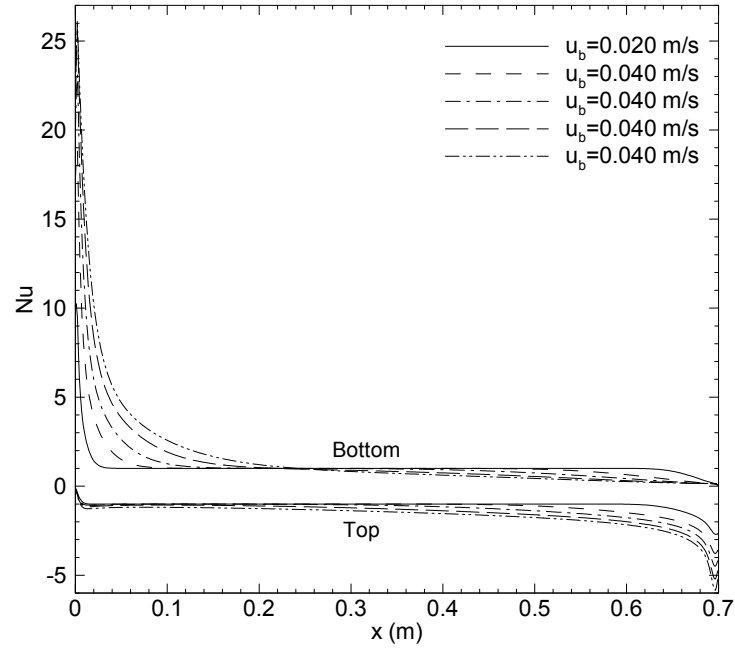


Fig. 15 Nu distribution on the top and bottom of flux layer (viscosity μ and bottom shear velocity $0.1 \text{ m}\cdot\text{s}^{-1}$)

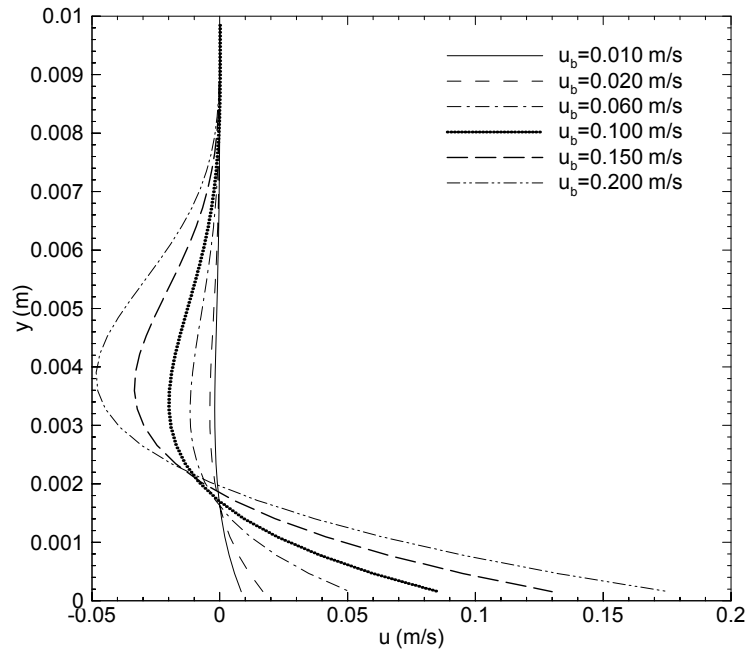


Fig. 16 Velocity profile across the domain thickness (centerline; flux a)

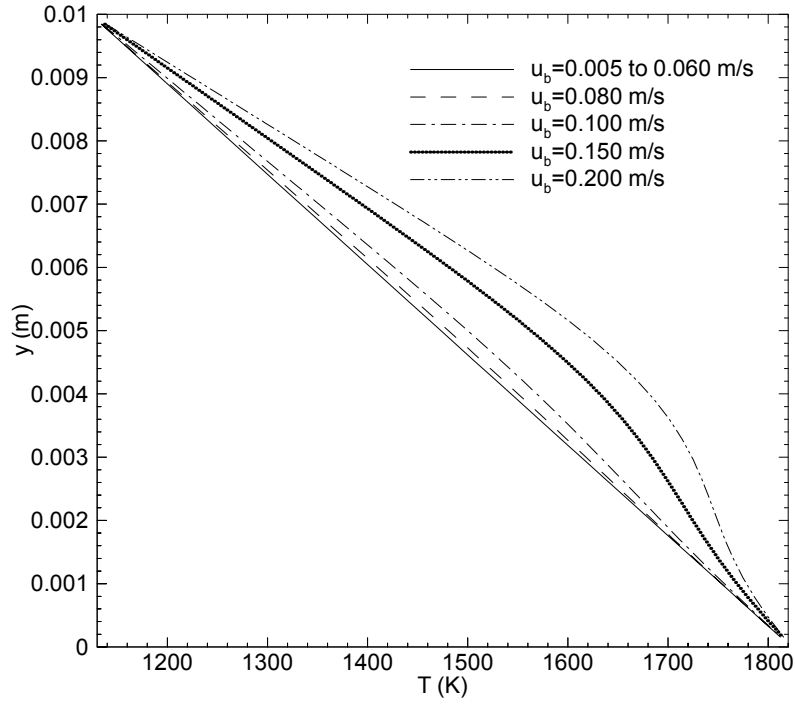


Fig. 17 Temperature profile across the domain thickness (centerline; flux a)

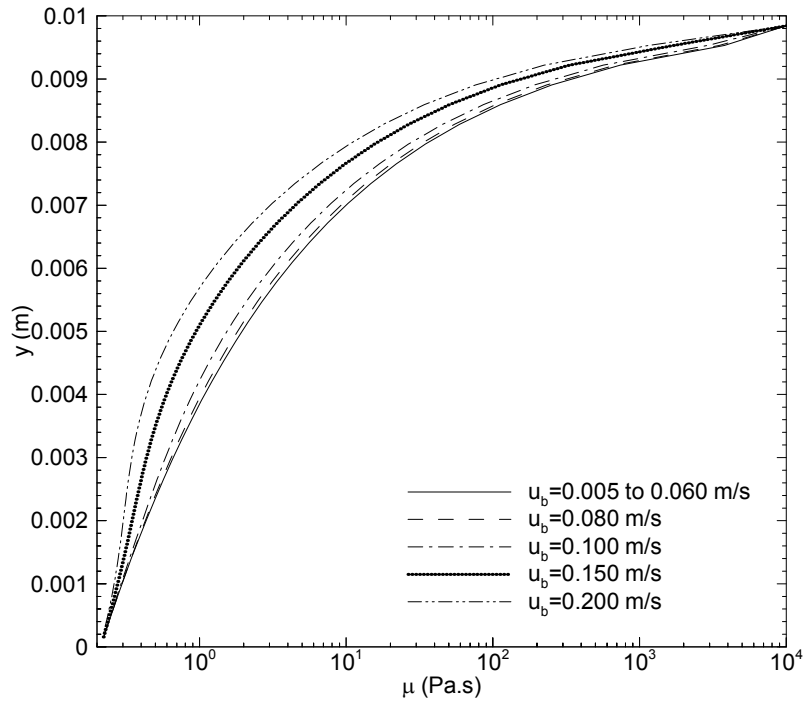


Fig. 18 Viscosity profile across the domain thickness (centerline; flux a)

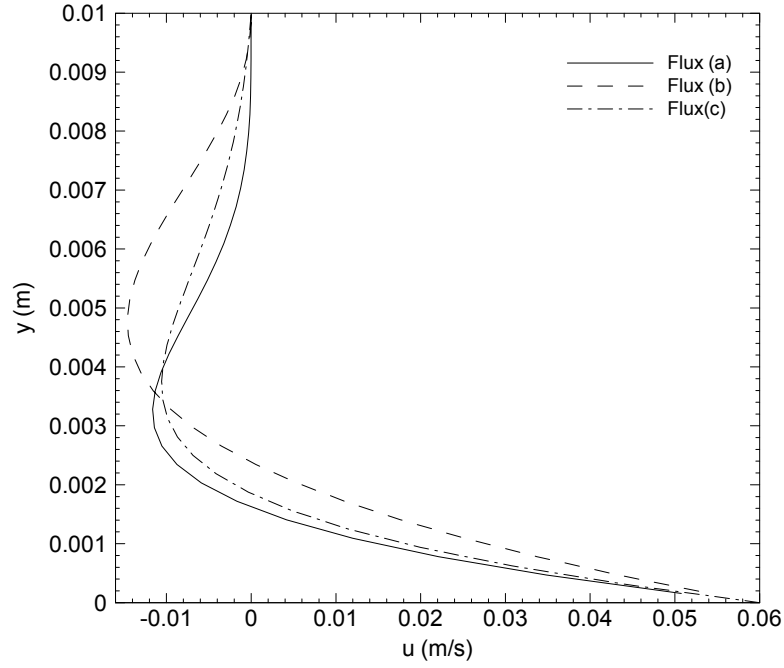


Fig. 19 Effect of flux viscosity on the velocity profile ($u_b=0.06 \text{ m}\cdot\text{s}^{-1}$)

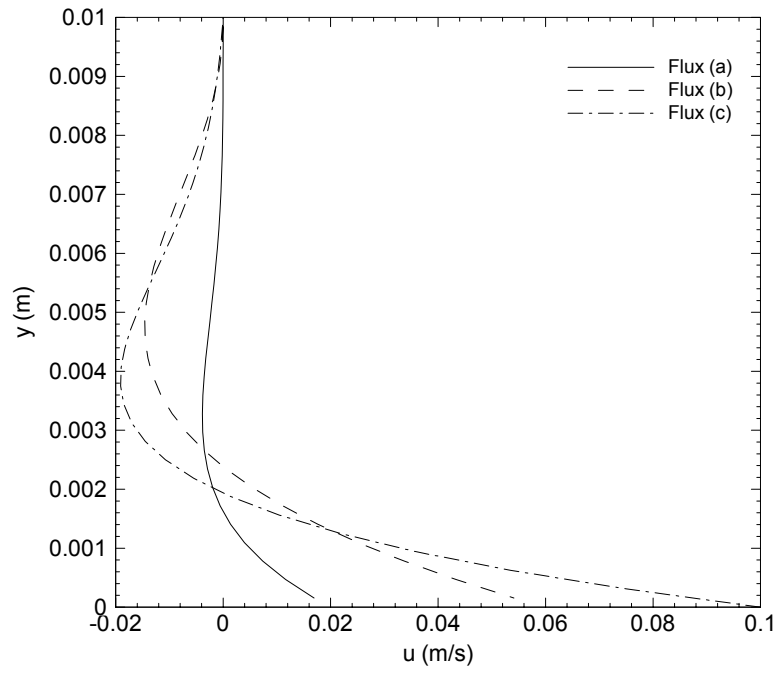


Fig. 20 Effect of flux viscosity on the velocity profile (interfacial shear stress equals $5 \text{ N}\cdot\text{m}^{-2}$)

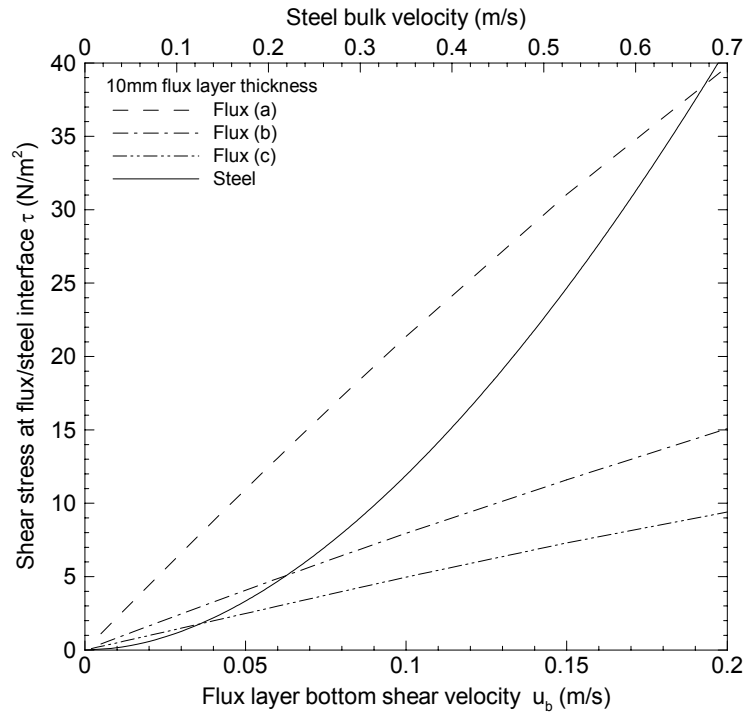


Fig. 21 Relationship between interfacial shear stress and flux/steel velocity

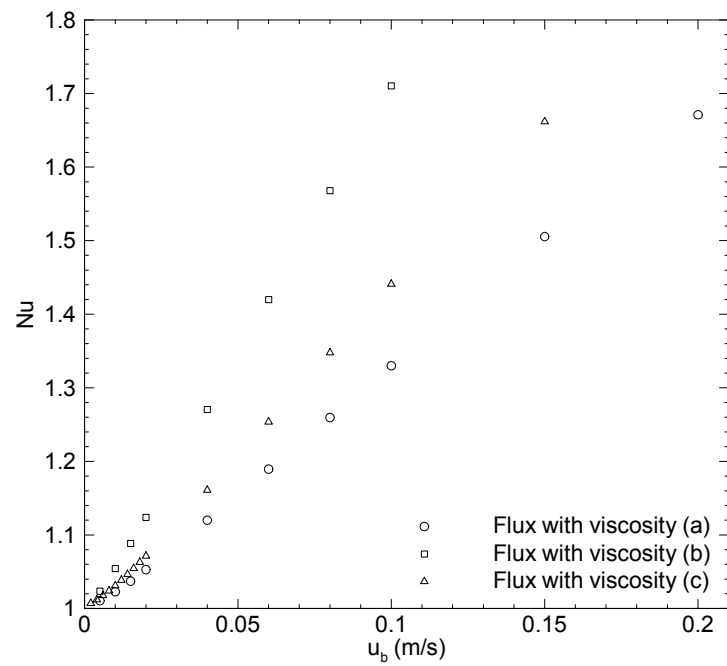


Fig. 22 Nu number as a function of bottom shear velocity

